Research Article

Ying Tong, Jiang Zhao, and Guo-zheng Quan*

Visualization of the damage evolution for Ti–3Al–2Mo–2Zr alloy during a uniaxial tensile process using a microvoids proliferation damage model

Abstract: Understanding the damage evolution of alloys during a plastic deformation process is significant to the structural design of components and accident prevention. In order to visualize the damage evolution in the plastic deformation of Ti–3Al–2Mo–2Zr alloy, a series of uniaxial tensile experiments for this alloy were carried out under the strain rates of 0.1–$10\,\mathrm{s}^{-1}$ at room temperature, and the stress–strain curves were achieved. On the other hand, the finite element (FE) models of these uniaxial tensile processes were established. A microvoids proliferation model, Gurson–Tvergaard–Needleman (GTN) damage model, was implanted into the uniaxial tensile models, and the simulated stress–strain curves corresponding to different GTN parameter combinations were obtained. Based on the simulated and experimental stress–strain curves, the GTN parameters of this alloy were solved by response surface methodology (RSM). The solved GTN parameters suggest that higher strain rate can enhance the proliferation and coalescence of microvoids. Furthermore, the uniaxial tensile tests over different strain rates were simulated using the solved GTN parameters. Then, the damage processes were visualized and evaluated. The result
shows that the degradation speed of this alloy is slow at the initial stage of the tensile deformation and then accelerates once the voids volume fraction reaches a critical value.

Keywords: GTN damage model, microvoids proliferation, FE simulation, Ti–3Al–2Mo–2Zr alloy

Nomenclature

CCD	central composite design
FE	finite element
GTN	Gurson–Tvergaard–Needleman
RSM	response surface methodology
VVF	voids volume fraction
Φ	yielding potential
σ_{eq}	von Mises equivalent stress
σ_{h}	hydrostatic stress
σ_{m}	equivalent stress of matrix material
q_1, q_2, q_3	calibration parameters of the damage model
f	voids volume fraction
f_0	initial voids volume fraction
f_{f}	final voids volume fraction
f_{c}	critical voids volume fraction
f_{u}^{*}	accelerating factor
$f_{\mathrm{nucleation}}$	voids volume fraction of the newly nucleated microvoids
f_{growth}	voids volume fraction of the growing microvoids
$\bar{\varepsilon}_{\mathrm{m}}^{\mathrm{pl}}$	microplastic strain
$\varepsilon_{\mathrm{kk}}^{\mathrm{p}}$	macroplastic strain
A	nucleation coefficient of microvoids
$\bar{\varepsilon}_{\mathrm{p}}$	equivalent plastic strain of matrix material
S_{N}	standard deviation
ε_{N}	equivalent plastic strain of microvoids
R_i	response variables ($i = 1, 2, ..., n$)
$\varepsilon_{\mathrm{E}}^{\mathrm{P}}$	experimental peak strain
$\varepsilon_{\mathrm{N}}^{\mathrm{P}}$	numerical peak strain

* **Corresponding author: Guo-zheng Quan,** Chongqing Key Laboratory of Advanced Mold Intelligent Manufacturing, School of Materials Science and Engineering, Chongqing University, Chongqing 400044, China; State Key Laboratory of Materials Processing and Die and Mould Technology, Huazhong University of Science and Technology, Wuhan 430074, China, e-mail: quangz3000@sina.com
Ying Tong: College of Intelligent Manufacturing and Automotive, Chongqing College of Electronic Engineering, Chongqing 401331, China
Jiang Zhao: Chongqing Key Laboratory of Advanced Mold Intelligent Manufacturing, School of Materials Science and Engineering, Chongqing University, Chongqing 400044, China

σ_E^P	experimental peak stress
σ_N^P	numerical peak stress
ε_E^F	experimental breaking strain
ε_N^F	numerical breaking strain
σ_E^F	experimental breaking stress
σ_N^F	numerical breaking stress

1 Introduction

Ti–3Al–2Mo–2Zr alloy is a near α titanium alloy with bits of β phase distributed on α matrix. It has wide application prospects in marine engineering, ship and chemical industry owing to its excellent combination properties, such as strong toughness, high fatigue resistance, middle strength and superior corrosion resistance [1,2]. This alloy is a prime candidate for Ti–6Al–4V alloy, mainly used in the skeleton parts and pressure vessels of underwater detectors [2]. When the detectors are subjected to violent shocks, these components will undergo destructive deformation to absorb the impact energy. Because of the high toughness and superior strength, this alloy is able to withstand huge deformation without breaking. In fact, the destructive deformation process is composed of three portions including elastic deformation, plastic deformation and damage degradation. Currently, the mechanical properties and the plastic deformation behaviors of this alloy have been reported [1,2]. However, little attention has been paid on the damage degradation behaviors of this alloy. It has been widely recognized that the damage degradation behavior of metals is of significance to the structural design and security evaluation of the components. Nevertheless, it is usually difficult to characterize the damage degradation process of metals because damage is essentially a nucleation and proliferation process of microvoids which cannot be detected directly [3]. Therefore, it is an important issue to find a suitable method to characterize the damage degradation behaviors of metals and to further understand the damage mechanism of this alloy.

Due to the fact that the essence of damage degradation is resulted from the nucleation and proliferation of microvoids, it is reasonable to characterize the degradation process of an alloy using the indicator of microvoids volume fraction. In order to achieve the evolution of this indicator during a certain deforming process, a reliable damage model is essential. Up till now, there have been a lot of damage models, such as coupled phenomenological models, uncoupled phenomenological models and micromechanical models [4]. The coupled or uncoupled phenomenological models have been increasingly applied in

industry due to the advantage of computation speed. However, the coefficient solution in the phenomenological models is dependent on the specified experimental conditions, and so such models cannot intrinsically describe the damage degradation behavior of materials [4]. It also means that the phenomenological models have a relatively higher tolerance in the computation of damage evolution. Nevertheless, a micromechanical model can solve this confused issue [5]. On the basis of the micromechanical theory, Gurson–Tvergaard–Needleman (GTN) model was developed [6], and until now it has been widely applied to describe the damage behaviors of materials, such as in aluminum alloy [7], titanium alloy [8], shape memory alloy [9], high strength steel [7], etc. Once the GTN model was figured out and planted into the finite element (FE) software, the volume fraction of microvoids can be derived in real time during a deforming process. Generally speaking, the damage degradation evolution of materials can be characterized by the FE simulation coupled with GTN model. In GTN model, there are four vital parameters that are closely related to the evolution mechanism of microvoids. According to the intrinsic concept of GTN model, the evolution of microvoids directly affects the yield behavior of materials, meanwhile the latter affects the former backward. That is to say, there exists a mapping relationship between the macroscopic yield behavior and the four GTN parameters. How to describe the mapping relationship is the key to solve the GTN parameters.

Response surface methodology (RSM) is suitable to clarify the chaotic mapping relationship. RSM seeks to identify the interior relationships between response variables and control factors through concise polynomial equations [10]. Compared with conventional fitting methods like orthogonal experimental method and polynomial fitting, RSM can achieve better fitting effect based on less experimental results. On the other hand, compared to intellectual algorithms, the fitting result of RSM is more intuitive and the fitted model is more convenient to be implanted into FE models. In addition, unlike the traditional regression method whose fitting effect significantly relies on the complexity of the independent variables, RSM can handle the complex function relationship even though sometimes there is more than one independent variable and these variables influence each other. More importantly, the higher fitting precision can be achieved because the non-significant solution set will be deleted during the regression calculation of RSM [11]. Naturally, RSM will be adopted in this work to solve the GTN parameters of Ti–3Al–2Mo–2Zr alloy.

In this work, a series of uniaxial tensile experiments were first performed to obtain the real stress–strain data. Then, the FE models of the uniaxial tensile processes

were established and the simulated stress–strain curves corresponding to different GTN parameter combinations were obtained. Based on the experimental stress–strain data and the simulated ones, the GTN parameters of Ti–3Al–2Mo–2Zr alloy were solved by RSM. As the uniaxial tensile FE models were simulated again using the solved GTN parameters, the damage degradation process of this alloy was characterized dynamically. Besides, the influence of strain rate on the damage degradation behavior was discussed in this work.

2 Methods and theoretical basis

2.1 Theoretical basis of GTN damage model

GTN model, as one of the classic microscopic mechanical models, has been widely used to describe the effect of ductile damage on the plastic yielding of materials [12]. The ductile damage process that contains the microvoids evolution can be schematically described as shown in Figure 1. When the material is deformed under a tensile stress, microvoids existing in the material begin to self-proliferate and expand. As the deformation continues, some microvoids begin to merge with each other, forming microcracks. Then, macrocracks come into being with the propagation and coalescence of the microcracks, resulting in dramatic performance degradation.

In the theory of GTN model, the impact of microvoids on the plastic yielding potential Φ of materials can be expressed as equation (1) [13].

$$\Phi = \left(\frac{\sigma_{eq}}{\sigma_m}\right)^2 + 2q_1 f^* \cosh\left(-\frac{3}{2}q_2\frac{\sigma_h}{\sigma_m}\right) - (1 + q_3 f^*)^2 = 0,$$

(1)

where σ_{eq} is the macro von Mises equivalent stress; σ_h is the macro hydrostatic stress; σ_m is the equivalent stress of matrix material; q_1, q_2 and q_3 are the calibration parameters of the model, and $q_3 = q_1^2$. Here q_1 and q_2 are 1.5 and 1, respectively, for this alloy [14]; f^* is the damage factor which can be expressed as the function of the voids volume fraction (VVF) as equation (2).

$$f^* = \begin{cases} f_0, & \text{if } f \leq f_c \\ f_c + \dfrac{f_u^\star - f_c}{f_f - f_c}(f - f_c), & \text{if } f > f_c, \end{cases}$$

(2)

where f represents the VVF; f_0 represents the initial VVF; f_f represents the final VVF, and the material will lose its loading capacity completely once f reaches to f_f; f_c represents the critical VVF, below which the voids will not proliferate and merge. f_u^* is the accelerating factor for the propagation and coalescence of microvoids. Usually, f_u^* can be calculated by q_1 as $f_u^* = q_1^{-1}$.

The VVF includes the contribution of newly nucleated microvoids and the growth of existing microvoids, and their relationships can be expressed as equation (3).

$$\begin{cases} df = df_{\text{nucleation}} + df_{\text{growth}} \\ df_{\text{nucleation}} = A d\bar{\varepsilon}_m^{pl} \\ df_{\text{growth}} = (1 - f)d\varepsilon_{kk}^p, \end{cases}$$

(3)

where df represents the total increment of VVF; $df_{\text{nucleation}}$ represents the increment of VVF that comes from newly nucleated microvoids; df_{growth} represents the increment of VVF that comes from the growth of existing microvoids. $d\bar{\varepsilon}_m^{pl}$ is the microplastic strain increment of the matrix material; $d\varepsilon_{kk}^p$ is the macroplastic strain increment. A is the nucleation coefficient of microvoids and it can be expressed as equation (4).
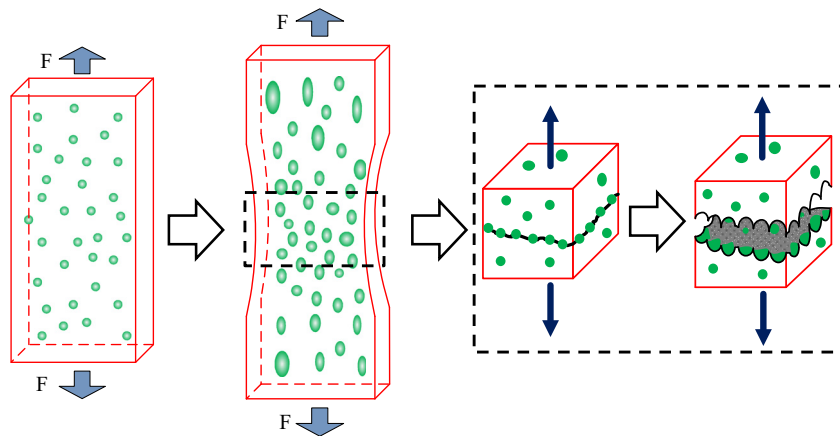

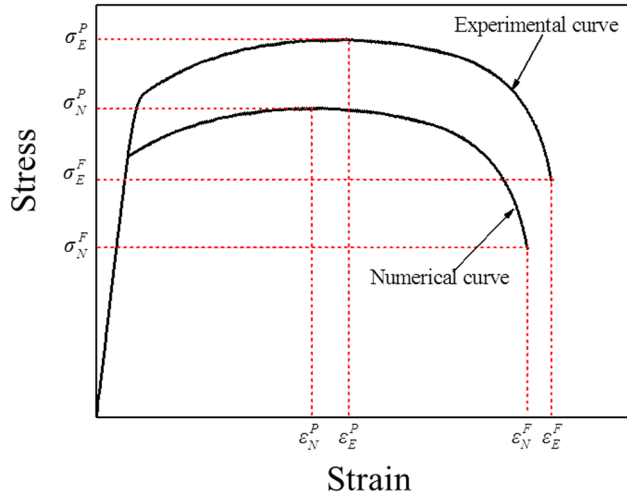**Figure 1:** Schematic illustration of ductile damage process.

Figure 2: Schematic description of the related indicators in the response variables of RSM.

$$A = \frac{f_{\text{nucleation}}}{S_N \cdot \sqrt{2\pi}} \cdot \exp\left[-\frac{1}{2} \cdot \left(\frac{\bar{\varepsilon}_p - \varepsilon_N}{S_N}\right)^2\right], \qquad (4)$$

where $f_{\text{nucleation}}$ represents the VVF of the newly nucleated microvoids; $\bar{\varepsilon}_p$ represents the equivalent plastic strain of matrix material; S_N represents the standard deviation and ε_N represents the equivalent plastic strain for the newly nucleated microvoids. According to refs [13,15,16], the values of ε_N and S_N can be taken as 0.3 and 0.1, respectively.

Based on the theoretical description of GTN damage model, the control parameters of GTN model include q_1, q_2, q_3, f_0, f_c, f_f, f_n, ε_N and S_N. Since some of the parameters have been obtained from references, the GTN parameters to be solved are f_0, f_c, f_f, f_n.

2.2 Theoretical basis of RSM

RSM, as a regression analysis method, was introduced by George E. P. Box and K. B. Wilson in 1951 [17]. It is dedicated to characterizing the quantified connection between the response variables and the independent variables. The main operation procedure of RSM is as follows. First, design a sequence of experiments to get the basic data for establishing response surface. Second, choose suitable regression equations to represent the response relationship. This relationship can be expressed as equation (5), where y represents the response variables and x_i ($i = 1, 2,…,n$) represent the factors.

$$y = f(x_1, x_2,…, x_n). \qquad (5)$$

Finally, fit the regression equation using the obtained experimental data by least square method, working out the coefficients in the regression equation. Usually, for the sake of saving calculation time and avoiding over-fitting, linear or quadratic polynomial functions are widely favored for the regression equations. Quadratic polynomial functions are adopted in the present work. The function of the response surface can be expressed as follows:

$$R = b_0 + \sum_{i=1}^{4} b_i X_i + \sum_{i=1}^{4} b_{ii} X_i^2 + \sum_{i=1}^{3}\sum_{j<i}^{4} b_{ij} X_i X_j, \qquad (6)$$

where R represents the response variables; b_0, b_i, b_{ii} and b_{ij} are the coefficients of response functions; X_i and X_j represent the independent variables.

2.3 Method for solving the GTN parameters based on RSM

One of the aims of this work is to figure out the values of GTN parameters. Hence, the GTN parameters can be regarded as the independent variables of the response surface. As introduced in the theory of GTN model, the GTN parameters determine the yielding behavior of alloys directly. Therefore, the indicators related to stress can be considered as the response variables. Since the stress–strain curve for a material gives the direct relationship between stress and deformation, the difference between experimental stress–strain curves and numerical ones can be defined as the response variables of RSM. The detailed expressions of the response values R are as follows:

$$\begin{cases} R_1 = |\varepsilon_E^P - \varepsilon_N^P| \\ R_2 = |\sigma_E^P - \sigma_N^P| \\ R_3 = |\varepsilon_E^F - \varepsilon_N^F| \\ R_4 = |\sigma_E^F - \sigma_N^F|, \end{cases} \qquad (7)$$

where ε_E^P and ε_N^P represent the experimental peak strain and numerical one, respectively; σ_E^P and σ_N^P represent the experimental peak stress and numerical one, respectively; ε_E^F and ε_N^F represent the experimental breaking strain and numerical one, respectively; σ_E^F and σ_N^F represent the experimental breaking stress and numerical one, respectively. These indicators are schematically shown in Figure 2. In Figure 2, the experimental stress–strain curve can be obtained from the tensile experiments, while the numerical stress–strain curve would be extrapolated from the FE simulation of the tensile processes.
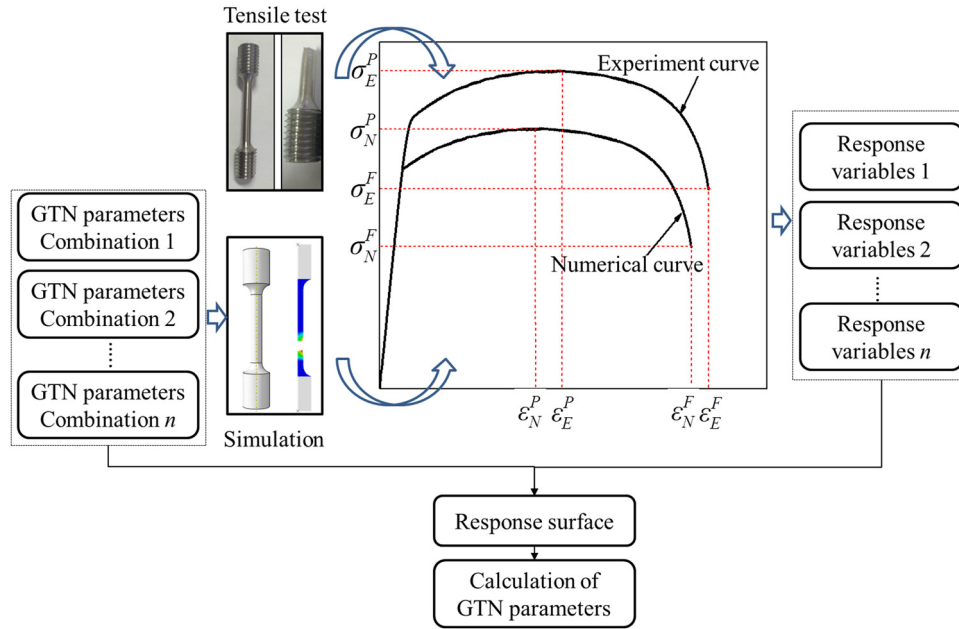
Figure 3: The solution procedures of GTN parameters.

Thereupon, for each GTN parameter combination, there will be a specific numerical stress–strain curve and a set of corresponding response value R. The solution process of the GTN parameters can be schematically described as shown in Figure 3. Based on the tensile tests, the experimental curves can be obtained. Then, simulate the tensile process using different GTN parameter combinations; meanwhile, acquire the corresponding response variables based on the difference between the experimental curves and numerical ones. Construct the response surface using the input GTN parameters and the corresponding response variables. Calculate the accurate GTN parameters based on the established response surface.

3 Experimental procedures

Based on the theory of RSM, it is prerequisite to acquire the experimental stress–strain data for establishing the response surfaces. Consequently, a sequence of uniaxial tensile tests for Ti–3Al–2Mo–2Zr alloy were performed in the strain rate range of 0.1–10 s^{-1} at room temperature.

The experimental details are as follows. First, four standard tensile specimens were separated from a block billet. The as-received material of the billet is as-cast Ti–3Al–2Mo–2Zr alloy with the relative chemical compositions as shown in Table 1. The size of the block billet is 100 mm^3 × 100 mm^3 × 140 mm^3, and its mass is 6.32 kg. Consequently, the mass density of this alloy was calculated as 4,510 kg·m^{-3} based on the density formula, where ρ is the mass density, m is mass and V represents the volume. The shape and size of the tensile specimens are shown in Figure 4. The uniaxial tensile experiments were carried out on a computer-controlled, servo-hydraulic WDW-100 tensile testing machine. Prior to the tensile experiments, the surfaces of the samples were grinded to avoid artificial microcracks. Subsequently, both ends of the samples were fixed on the clamps of the tensile machine. The experimental setup with a tensile specimen mounted in terms of grip setup is shown in Figure 5. Then, the specimens were stretched to break with a specific strain rate. During the tensile tests, the load and distance data were monitored and recorded in real time by a computer control data acquisition system.

Table 1: Chemical composition of Ti–3Al–2Mo–2Zr alloy (wt%)

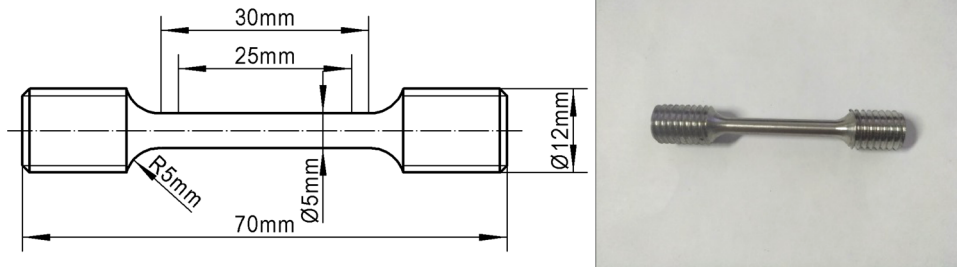| Element	Al	Mo	Zr	Fe	Si	C	N	H	O	Ti
Content (wt%)	3	2	1.9	0.07	0.04	0.01	0.008	0.001	0.11	Bal.

Figure 4: The shape and size of the tensile samples.

From the load-distance data, the nominal stress–strain can be obtained by $\sigma_N = F/S$ and $\varepsilon_N = d/D_0$, where σ_N represents the nominal stress; F is the applied load; S is the cross sectional area of the specimens; ε_N is the nominal strain; d is the recorded distance; D_0 is the initial length of the specimens. Further, the nominal stress–strain data were converted into true stress–strain data based on the formulas: $\sigma_T = \sigma_N(1 + \varepsilon_N)$ and $\varepsilon_T = \ln(1 + \varepsilon_N)$, where σ_T is the true stress and ε_T is the true strain [18]. The true stress–strain curves for Ti−3Al−2Mo−2Zr alloy under varying strain rates are exhibited in Figure 6. In Figure 6, there is a linear stage on each stress–strain curve, i.e., the elastic stage of the material. Consequently, the Young's modulus of this alloy can be evaluated by linearly fitting the elastic stage of the stress–strain curves, and the result is 115 GPa. Besides, it can be seen from Figure 6 that the strain rate has little impact on the variety of peak stress, while it has obvious influence on the breaking stress, peak strain and breaking strain. With increase in strain rate, the values of both the peak strain and breaking strain decrease. These phenomena may be caused by the harder deformation coordination under higher strain rate. It is well-known that the multi-crystal plastic deformation depends on dislocation glide and the rotation of grains. At higher strain rate, there is no sufficient time for the rotation of deforming grains, which can more easily lead to local stress concentration and non-uniform plastic deformation. Moreover, at higher strain rate, there is no sufficient time for the energy dissipation of material via plastic deformation. These reasons increase the fracture tendency of material over high strain rate. As for the peak stress, strain rate has no obvious impact on its variety because the peak stress of materials depends only on the inherent bearing capacity of the materials.

After the tensile experiments, the fracture morphologies of the tensile specimens were characterized on a VEGA3 TESCAN scanning electron microscope. The experimental accelerating voltage was set as 20 kV and the work distance was set as 26 mm.
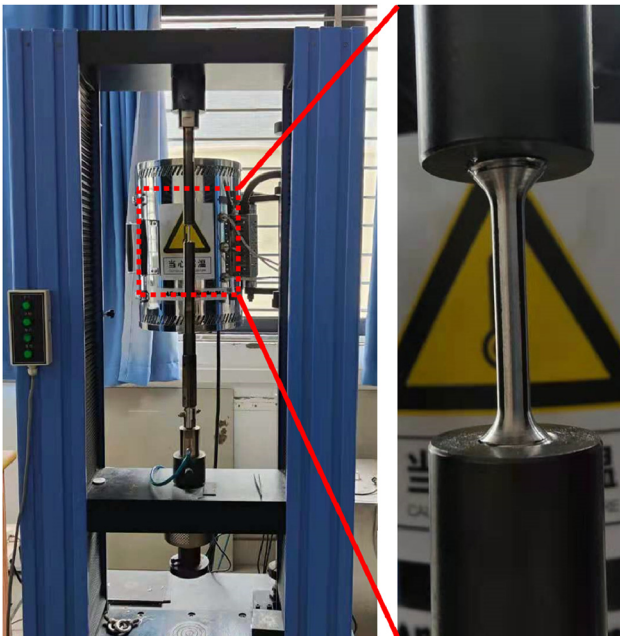

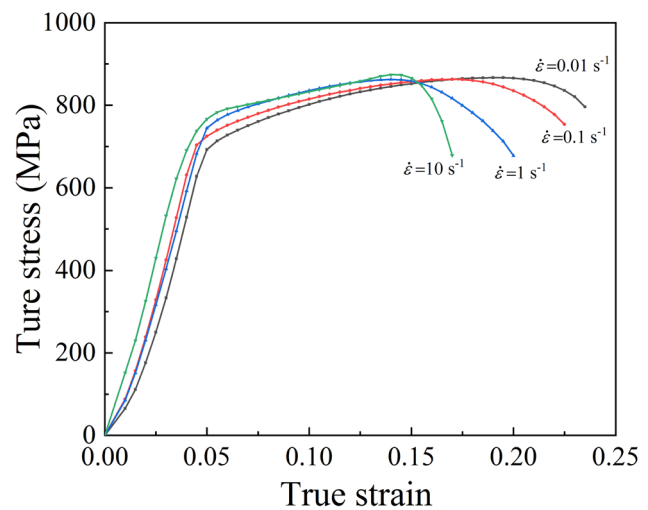**Figure 5:** The setup of the uniaxial tensile experiments.

Figure 6: The true stress–strain curves of Ti−3Al−2Mo−2Zr alloy under different strain rates.

4 Results and discussion

4.1 Numerical model of uniaxial tensile process

To calculate the response variables corresponding to various GTN parameters, it is necessary to carry out the numerical simulation of the uniaxial tensile processes. The simulation is carried out on the FE platform ABAQUS. For saving simulation time, the FE model of the uniaxial tensile process was simplified as an axisymmetric model. The simplified tensile model was meshed with the quadrilateral element (CAX4R), and 657 nodes and 548 elements were obtained. The simplified model and the boundary condition of the tensile simulation are shown in Figure 7. In order to ensure that the strain rate in the numerical simulation is consistent with that in the tensile experiments, the tensile speed exerted on the specimens should be calculated by $v = l_0 \dot{\varepsilon} \exp(\dot{\varepsilon} t)$, where l_0 represents the gauge length of the specimens, 25 mm here. GTN damage model is applied in the tensile simulation. The mechanical property parameters that are required for the tensile simulation of Ti–3Al–2Mo–2Zr alloy are presented in Table 2 [19,20]. According to the tensile experiments, it has been found that the deformation span is very short for the tensile process of this alloy. Therefore, in order to obtain more details on the damage evolution during the tensile process, the simulation is performed using the explicit analysis arithmetic with an automatic time step. The computational cost for the FE simulation is a personal computer with an eight-core processer. Four threads were applied during the computation of the uniaxial tensile FE model. The computational time lasts about four hours for each uniaxial tensile process.

4.2 Solution of the GTN parameters based on RSM

In order to construct the response surface of GTN parameters versus response variables, a series of simulation schemes need to be designed. Central composite design
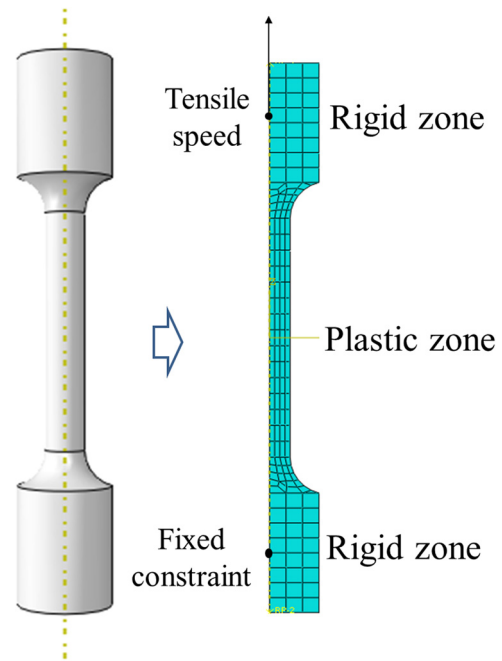

Figure 7: FE model and boundary condition of the uniaxial tensile simulation.

(CCD) method is applied in this work to design the simulation schemes. Based on the CCD method, a four-factors-three-levels simulation scheme was designed, as shown in Table 3. These factors correspond to the GTN parameters to be solved, i.e., the initial VVF (f_0), critical VVF (f_c), nucleation VVF (f_N) and the final VVF (f_f).

Taking the strain rate of $0.01\,\text{s}^{-1}$ for instance, the detailed solution process of GTN parameters will be demonstrated. First, the uniaxial tensile process was simulated using the designed GTN parameter combination in Table 3 under the strain rate of $0.01\,\text{s}^{-1}$. The response values corresponding to different GTN parameters were calculated according to the previously introduced procedure, and the results were recorded as shown in Table 3.

Based on the factors and corresponding response values in Table 3, the final functions of the response surfaces were achieved by least squares method. The expressions are shown in equation (8).

Table 2: The mechanical property parameters of Ti–3Al–2Mo–2Zr alloy [19,20]

Mass Density (kg·m^{-3})	Young's modulus (GPa)	Poisson's ratio	Yield strength (MPa)	Breaking strength (MPa)
4,510	115	0.34	640	720

$$R_1 = 6.04 - 84.54 \times f_0 - 108.93 \times f_n - 7.43 \times f_c$$
$$+ 9.84 \times f_f - 209.54 \times f_0 \times f_n$$
$$- 655.75 \times f_0 \times f_c + 42.64 \times f_0 \times f_f$$
$$- 19.86 \times f_n \times f_c - 26.03 \times f_n \times f_f$$
$$+ 54.08 \times f_c \times f_f + 8708.41 \times f_0^2$$
$$+ 990.57 \times f_n^2 + 12.54 \times f_c^2 - 32.78 \times f_f^2,$$

(8.1)

$$R_2 = 755.71 + 22835.48 \times f_0 + 11.89 \times f_n + 1.9 \times f_c$$
$$+ 0.32 \times f_f - 1{,}875 \times f_0 \times f_n$$
$$- 1977.40 \times f_0^2 - 19.77 \times f_n^2 - 12.66 \times f_c^2$$
$$- 0.79 \times f_f^2,$$

(8.2)

$$R = 33.46 + 427.43 \times f_0 + 58.96 \times f_n + 18.35 \times f_c$$
$$- 18.73 \times f_f - 329.5 \times f_0 \times f_n$$
$$- 1124.6 \times f_0 \times f_c - 440.85 \times f_0 \times f_f$$
$$- 85.46 \times f_n \times f_c - 4.44 \times f_n \times f_f$$
$$+ 66.12 \times f_c \times f_f + 38822.32 \times f_0^2 - 267.25$$
$$\times f_n^2 - 199.46 \times f_c^2 + 27.88 \times f_f^2,$$

(8.3)

$$R_4 = 3499.34 - 4.65 \times 10^6 \times f_0 + 6.1 \times f_n$$
$$- 7.3 \times 10^5 \times f_c + 1.58 \times 10^5 \times f_f$$
$$+ 1.1 \times 10^7 \times f_0 \times f_n + 6.3 \times 10^6$$
$$\times f_0 \times f_c + 4.1 \times 10^6 \times f_0 \times f_f$$
$$+ 1.3 \times 10^6 \times f_n \times f_c + 4 \times 10^5 \times f_n \times f_f$$
$$- 4.5 \times 10^5 \times f_c \times f_f + 4.94 \times 10^8 \times f_0^2$$
$$- 6.67 \times 10^6 \times f_n^2 + 4.67 \times 10^6 \times f_c^2$$
$$- 3.43 \times 10^5 \times f_f^2.$$

(8.4)

Due to the fact that the response variables R in equation (8) represent the difference between experimental and simulated stress–strain curves, the minimum R-values correspond to the most possible GTN parameter values. In other words, the closer the input GTN parameter is to the actual values, the smaller the response variables R-values will be. Consequently, the GTN parameters will be solved by searching for a suitable parameter combination that makes the response variables reach the minimum almost simultaneously. Considering the significant difference among R_1, R_2, R_3 and R_4, the response variables

Table 3: Simulation scheme and response values under the strain rate of 0.01 s^{-1}

Number	Factors				Response values			
	f_0	f_N	f_c	f_f	R_1	R_2	R_3	R_4
1	0.003	0.08	0.075	0.2	3.718	844.700	5.163	1689.200
2	0.001	0.04	0.05	0.1	3.692	799.000	4.900	1661.500
3	0.001	0.04	0.1	0.3	3.707	799.000	4.336	1760.400
4	0.005	0.08	0.05	0.1	3.658	890.000	5.544	984.000
5	0.003	0.04	0.075	0.2	3.715	844.500	3.981	4670.210
6	0.001	0.08	0.1	0.3	3.818	799.300	4.422	4524.150
7	0.005	0.06	0.075	0.2	3.094	890.000	4.650	4055.700
8	0.005	0.04	0.1	0.3	3.428	890.000	3.599	3886.990
9	0.001	0.08	0.1	0.1	3.758	799.300	5.134	1034.500
10	0.003	0.06	0.075	0.2	3.328	844.600	4.634	3295.640
11	0.001	0.04	0.05	0.3	3.188	799.000	3.509	6129.780
12	0.003	0.06	0.075	0.3	2.983	844.600	4.900	1609.900
13	0.005	0.08	0.05	0.3	2.988	890.000	4.756	9433.700
14	0.003	0.06	0.05	0.2	3.448	844.600	4.758	11099.544
15	0.005	0.08	0.1	0.1	3.318	890.000	5.131	3373.140
16	0.005	0.08	0.1	0.3	3.328	890.000	4.268	11299.895
17	0.003	0.06	0.075	0.1	3.002	844.600	5.017	3214.460
18	0.001	0.04	0.1	0.1	3.515	799.000	3.963	2678.190
19	0.001	0.08	0.05	0.3	3.335	799.300	4.761	7737.760
20	0.003	0.06	0.1	0.2	3.208	844.600	4.352	6431.840
21	0.005	0.04	0.1	0.1	3.183	890.000	4.321	2189.140
22	0.005	0.04	0.05	0.3	3.094	890.000	3.614	10281.530
23	0.005	0.04	0.05	0.1	3.185	890.000	5.192	657.400
24	0.001	0.08	0.05	0.1	3.726	799.300	5.574	77.000
25	0.001	0.06	0.075	0.2	3.616	799.200	4.398	11588.561

should be replaced by dimensionless variables R_1', R_2', R_3' and R_4', as shown in equation (9).

$$\begin{cases} R_1' = \dfrac{R_1}{\varepsilon_E^P} \\ R_2' = \dfrac{R_2}{\sigma_E^P} \\ R_3' = \dfrac{R_3}{\varepsilon_E^F} \\ R_4' = \dfrac{R_4}{\sigma_E^F}. \end{cases} \qquad (9)$$

Subsequently, the GTN parameters were solved by inputting the modified response functions into Matlab software. The solved GTN parameters are as follows: $f_0 = 0.005$, $f_N = 0.0412$, $f_c = 0.0686$ and $f_f = 0.3016$.

Repeating the above calculation procedures, the GTN damage parameters at different strain rates were figured out, and the results were recorded as shown in Table 4.

According to Table 4, the strain rate has significant influence on the GTN parameters, especially for the final

Table 4: The solved GTN parameters at different strain rates

Strain rate	f_0	f_N	f_c	f_f
0.01	0.0050	0.0412	0.0686	0.3016
0.1	0.0046	0.0536	0.0725	0.2357
1	0.0039	0.0698	0.0749	0.1964
10	0.0042	0.0737	0.0751	0.1481

VVF. With the increase in the strain rate, the value of the final VVF decreases. Whereas, the nucleation VVF and critical VVF increase with the increase in the strain rate. As for the initial VVF, there exists little discrepancy under different strain rates.

When the specimens deform under high strain rate, the slip speed of dislocations is rapid. The deformation will not be coordinated, leading to local stress concentration on the matrix. The high interior stress will stimulate the deformation and expansion of the microvoids [21,22]. In addition, as the deformation process continues, the microvoids will be more easy to connect under the
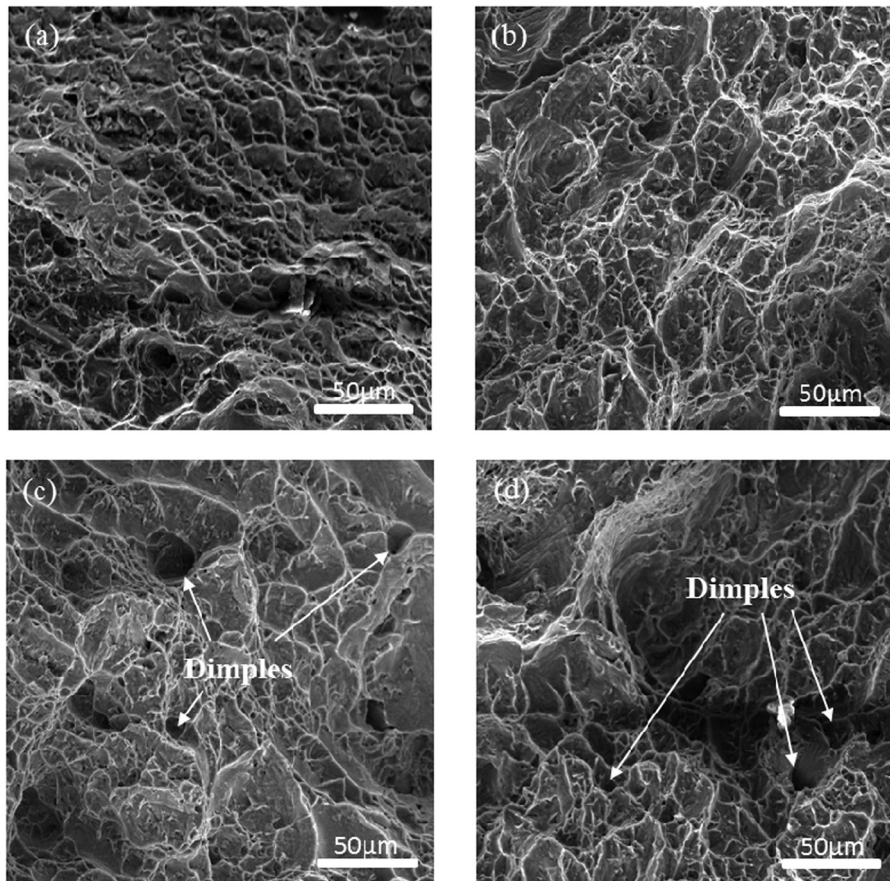

Figure 8: The scanning electron micrographs of the fracture morphologies for the tensile specimens deformed at different strain rates: (a) $0.01\,s^{-1}$, (b) $0.1\,s^{-1}$, (c) $1\,s^{-1}$, and (d) $10\,s^{-1}$.

concentrated interior stress. When the necking occurs, the VVF reaches a critical value. The critical VVF is higher at high strain rate because the nucleation and expanding rate of voids is quicker at high strain rate. It is remarkable that the final VVF is smaller at higher strain rate, because there is no sufficient time for the nucleation and growth of the microvoids. For clearly displaying the impact mechanism of strain rate on the voids evolution, the scanning electron micrographs of the fracture morphologies for the tensile specimens are shown in

Figure 8. There are obvious dimples in Figure 8 and it means that ductile damage is the dominant degradation mechanism for this alloy under the strain rate range of $0.1–10\ s^{-1}$. There are fine dimples in Figure 8a and b. In Figure 8c and d, the dimples are coarse and sparse. Therefore, a conclusion can be drawn that the higher strain rate contributes to the expansion and coalescence of the microvoids; meanwhile, the number of the microvoids will be less under high strain rate because of the insufficient deformation time.
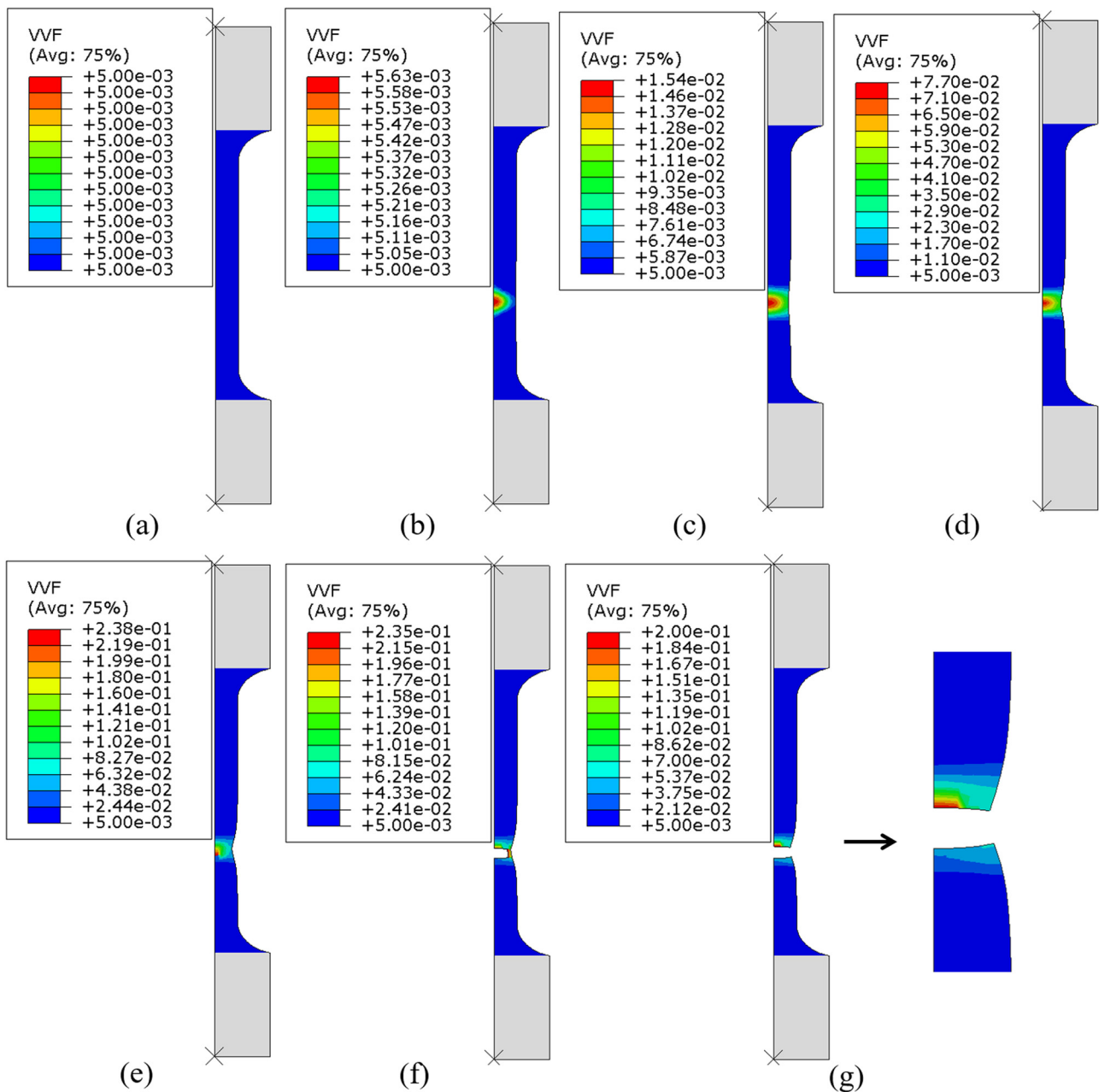

Figure 9: The distribution of void volume fraction at the true strain of (a) $0\ s^{-1}$, (b) $0.05\ s^{-1}$, (c) $0.1\ s^{-1}$, (d) $0.15\ s^{-1}$, (e) $0.2\ s^{-1}$, (f) $0.229\ s^{-1}$, and (g) $0.23\ s^{-1}$.

4.3 Characterization of the damage degradation behavior of Ti–3Al–2Mo–2Zr alloy

In order to dynamically characterize the damage degradation process of Ti–3Al–2Mo–2Zr alloy, the uniaxial tensile processes were numerically simulated using the solved GTN parameters. Subsequently, the damage degradation behaviors of Ti–3Al–2Mo–2Zr alloy were discussed taking

the strain rate of $0.01\,\mathrm{s^{-1}}$ as an example. Figure 9 shows the distribution and evolution of the VVF in the tensile process. According to the simulation results, it can be seen that the microvoids nucleate in the interior of the specimen at the beginning of the tensile process, and the microvoids begin to proliferate and propagate with the proceeding tensile deformation. When the true strain reaches $0.1\,\mathrm{s^{-1}}$, necking occurs and the VVF increases to a critical level. With the ongoing tensile deformation, the
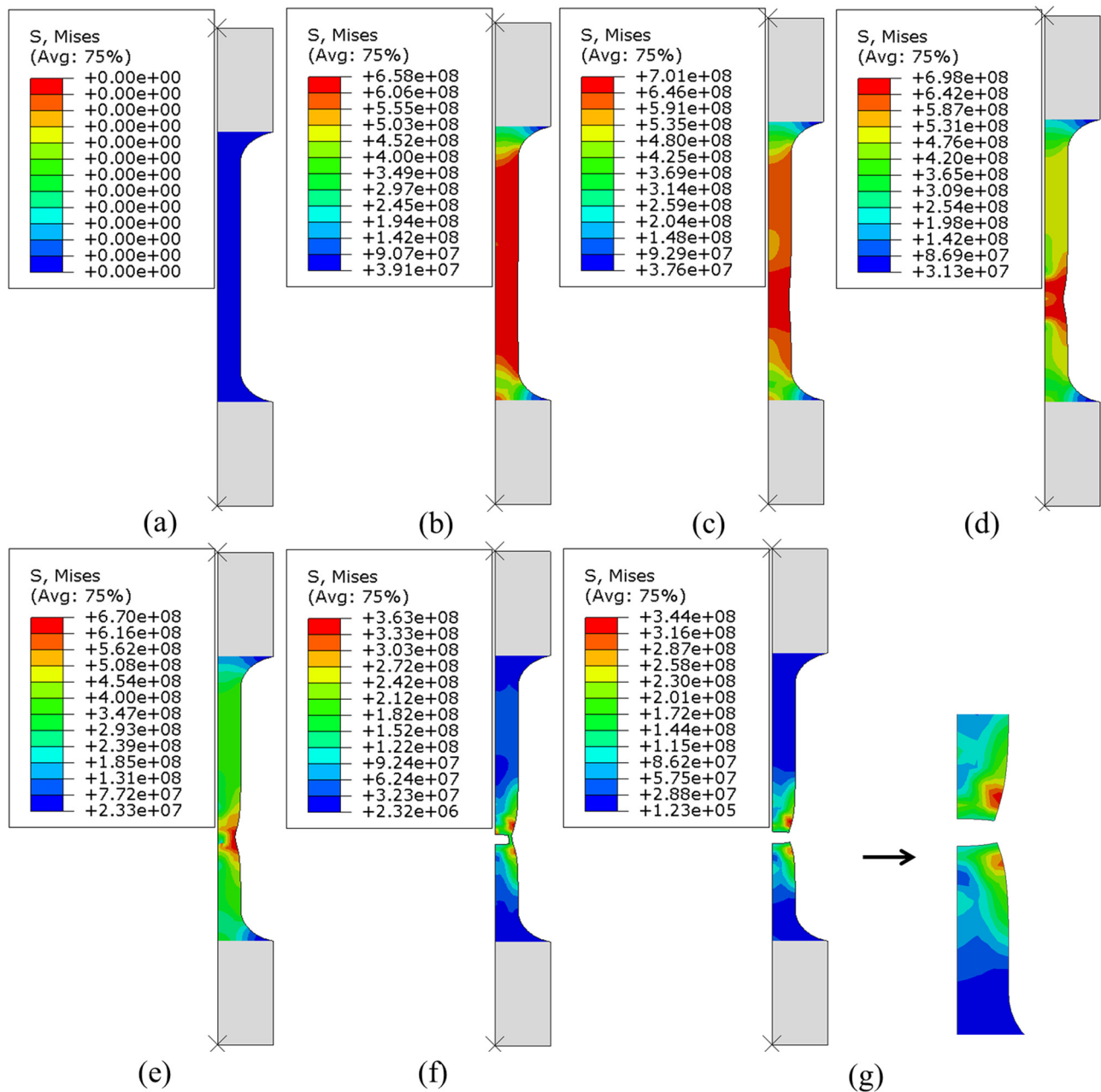

Figure 10: The distribution of Mises equivalent stress at the true strain of (a) $0\,\mathrm{s^{-1}}$, (b) $0.05\,\mathrm{s^{-1}}$, (c) $0.1\,\mathrm{s^{-1}}$, (d) $0.15\,\mathrm{s^{-1}}$, (e) $0.2\,\mathrm{s^{-1}}$, (f) $0.229\,\mathrm{s^{-1}}$, and (g) $0.23\,\mathrm{s^{-1}}$.

VVF keeps increasing until the maximum VVF arrives at the final VVF (f_f). At this time, the specimen loses its overall loading capacity. The fracture position of the tensile specimen in the simulation is in good agreement with the experimental results.

In order to understand the damage process deeply, it is essential to analyze the stress evolution of the tensile process. Figure 10 shows the simulation result of equivalent Mises stress in the tensile process. It is obvious that the distribution of the equivalent stress is uniform at the initial stage of the tensile process. When the true strain reaches $0.1\,\mathrm{s}^{-1}$, the equivalent stress shows a non-uniform distribution. As the deformation continues, the non-uniform stress distribution becomes more and more obvious, and higher stress concentrates in the middle and lower part of the specimen. It has been introduced in the theory of the GTN model that the stress concentration will promote the proliferation of microvoids. On the contrary, the increase in the VVF will make the loading capacity of materials decrease. Consequently, the mutual improvement between
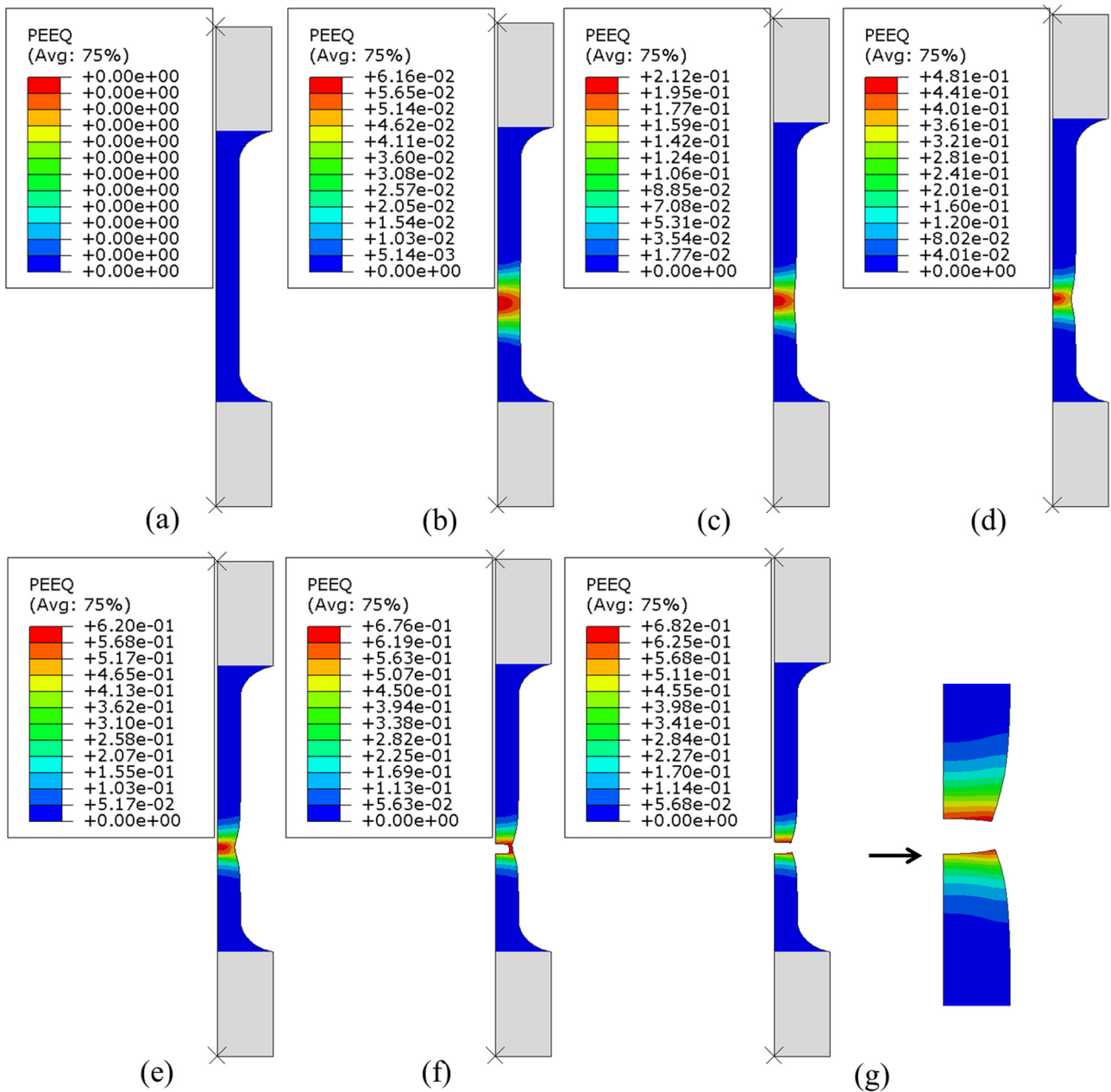

Figure 11: The distribution of equivalent plastic strain at the true strain of (a) $0\,\mathrm{s}^{-1}$, (b) $0.05\,\mathrm{s}^{-1}$, (c) $0.1\,\mathrm{s}^{-1}$, (d) $0.15\,\mathrm{s}^{-1}$, (e) $0.2\,\mathrm{s}^{-1}$, (f) $0.229\,\mathrm{s}^{-1}$, and (g) $0.23\,\mathrm{s}^{-1}$.

stress concentration and microvoids proliferation leads to the equivalent stress decrease in the later stage of the tensile deformation.

In order to reveal the relationship between damage degradation and plastic deformation, the simulation results of equivalent plastic strain are presented in Figure 11. It is apparent that the plastic deformation zone is very small, and it mainly occurs at the middle and lower part of the specimen, where VVF is higher. The evolution of equivalent plastic strain indicates that the strain is sensitive to the

damage degradation of this alloy. Comparing Figure 11a–g with each other, it can be found that the strain distribution is relatively uniform at the initial stage of the tensile deformation. When the true strain reaches 0.1 s⁻¹, the plastic deformation area intends to contract inside because the VVF is higher at the center of the specimen; meanwhile, necking appears at the area where the equivalent plastic strain is high. Generally, deforming is more easy at the areas with higher VVF because the deformation resistance is lower. When the true strain reaches 0.15 s⁻¹, the maximum
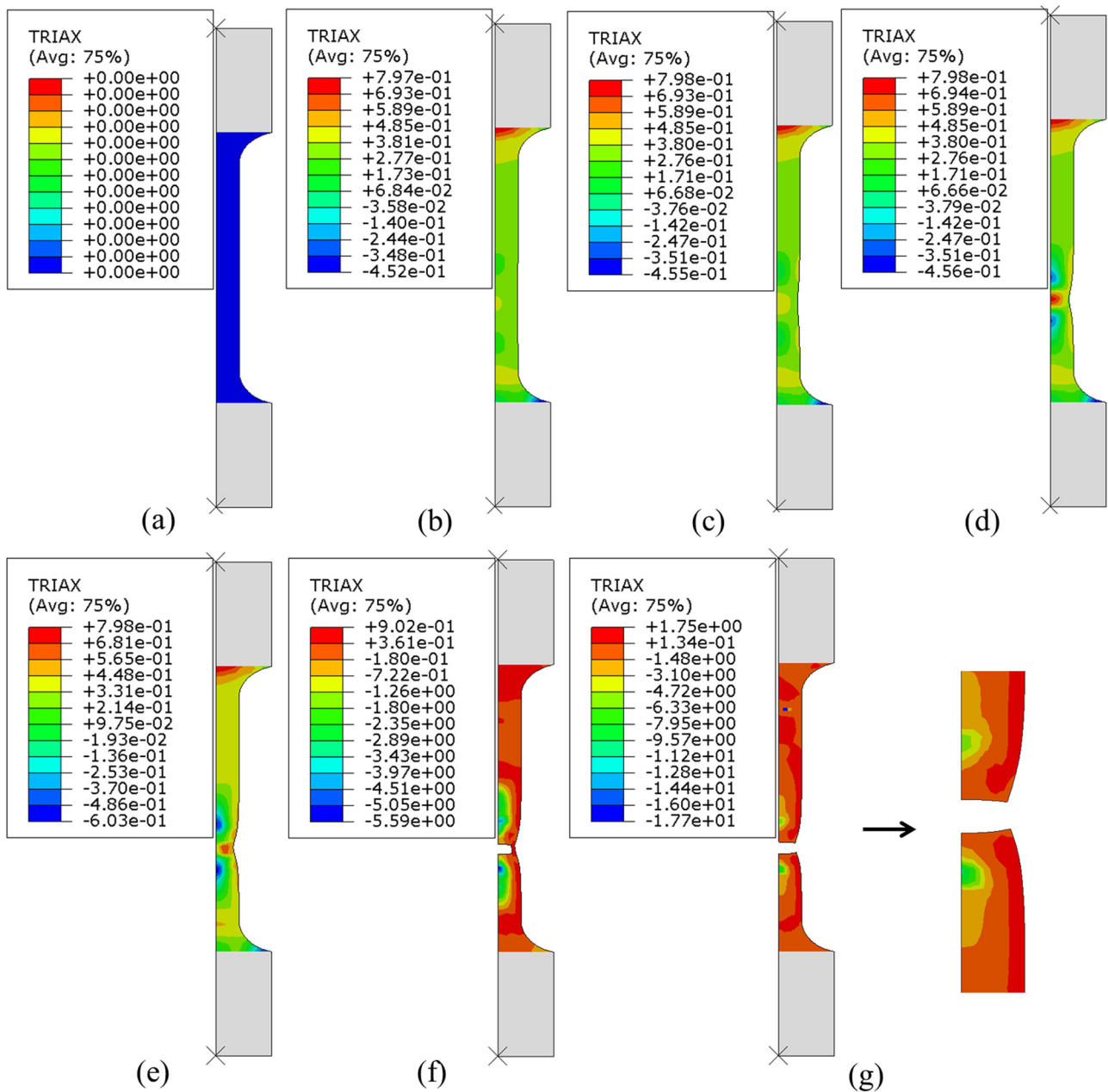

Figure 12: The distribution of stress triaxiality at the true strain of (a) 0 s⁻¹, (b) 0.05 s⁻¹, (c) 0.1 s⁻¹, (d) 0.15 s⁻¹, (e) 0.2 s⁻¹, (f) 0.229 s⁻¹, and (g) 0.23 s⁻¹.

of plastic strain keeps basically stable. Further tensile deformation will make the specimen break off.

Not only the equivalent stress and plastic strain, but also the stress state is a key impact factor for the damage degradation behaviors of materials. Stress triaxiality is widely applied to represent the stress state of materials. High stress triaxiality values correspond to the tensile stress state, while low stress triaxiality values correspond to the compressive stress state. As for uniaxial tensile stress state, the stress triaxiality value is close to 0.3. Figure 12 exhibits the distribution and evolution of the stress triaxiality in the tensile process of Ti−3Al−2Mo−2Zr alloy. It is obvious that the stress triaxiality is 0.3 in most areas of the tensile specimen. The stress triaxiality at the fracture position is relatively high, which means the failure mechanism of this alloy is ductile damage. It is in agreement with the result that is observed from the EBSD images. More interestingly, the variety of stress triaxiality is complex at the fracture position. The center of the fracture position shows a higher stress triaxiality value, while the vicinities along the tensile axis show a lower stress triaxiality value. It indicates that the damage intents to initiate at the center of the specimen, and then expand along the direction perpendicular to the tensile axis. In addition, there is a visible change in the stress triaxiality distribution at the true strain of $0.1\,\mathrm{s}^{-1}$. This suggests that the microvoids begin to proliferate and expand quickly at the true strain of $0.1\,\mathrm{s}^{-1}$; meanwhile, the VVF reaches a critical value.

In summary, the VVF is closely related to the stress, strain and stress state of the materials. The existence of microvoids will lead to the stress concentration, uneven plastic deformation and the change in local stress state. And the latter will contribute to the increase in VVF in return. This is the damage degradation process of materials during the uniaxial tensile deformation.

Since the evolution of VVF in the tensile process has been visualized by FE simulation, the degradation process of this alloy can be evaluated dynamically. Here the damage degradation degree is defined as the percentage of the current VVF to final VVF. Correspondingly, the damage degradation curves of Ti−3Al−2Mo−2Zr alloy at different strain rates were plotted as shown in Figure 13. According to Figure 13, it is apparent that all the degradation curves show a similar tendency, and the degradation speed is faster at higher strain rate. This point can be explained by the damage mechanism of this alloy. As discussed in the above Sections, the nucleation and proliferation of the microvoids is the dominant damage mechanism for this alloy. Therefore, in the early stage of the deformation, the progress of degradation process is slow because of the low nucleation speed of microvoids. In the middle and later stages of the tensile deformation, the degradation is faster because the nucleation and expansion of microvoids are promoted once the VVF reaches the critical value (f_c). Particularly, the promoting effect is enhanced under higher strain rates because the stress concentration and uneven plastic deformation is more severe at higher strain rate.

5 Conclusion

The damage degradation behaviors of Ti−3Al−2Mo−2Zr alloy have been studied by the FE simulation combined with uniaxial tensile experiments at the strain rate range of 0.1–$10\,\mathrm{s}^{-1}$. And the following conclusions have been drawn.

(1) For Ti−3Al−2Mo−2Zr alloy, the GTN parameters corresponding to different strain rates were worked out based on RSM.

(2) Strain rate has significant influence on the GTN parameters. Higher strain rate contributes to the growth and coalescence of microvoids. In addition, the final VVF is lower at the higher strain rate because of the insufficient deformation time.

(3) The evolution of microvoids volume fraction was visualized based on a FE platform and the solved GTN parameters. The damage degradation curves of Ti−3Al−2Mo−2Zr alloy were drawn out. The degradation speed of this alloy is slow at the beginning stage of the tensile process and then accelerates once the VVF reaches a critical value.
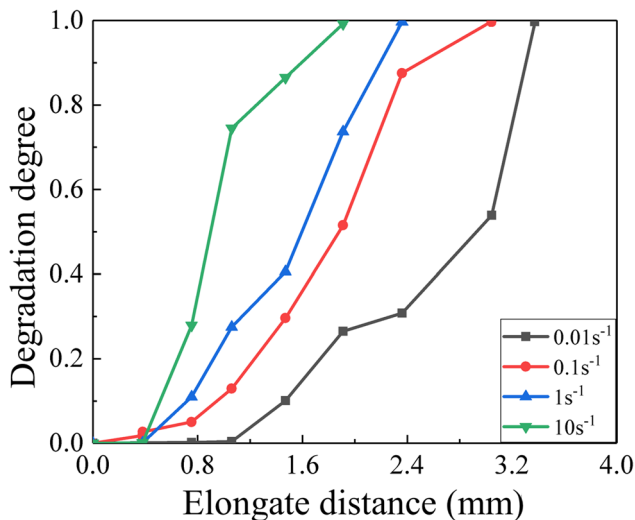

Figure 13: The damage degradation curves of Ti−3Al−2Mo−2Zr alloy at different strain rates.

Author contributions: Ying Tong: writing and funding. Jiang Zhao: experiment and data. Guozheng Quan: conception and funding.

Conflict of interest statement: There is no interests conflict with others.

Data available statement: All authors can confirm that all data used in this article can be published in the Journal "High Temperature Materials and Processes".

References

[1] Fan, J. Hot compression simulation of Ti3Al alloy based on DEFORM-3D. *Applied Mechanics and Materials*, Vol. 101, 2012, pp. 240–244.

[2] Li, C., H. Ding, Y. Zhao, and L. Zhou. A study on mechanical behavior and microstructural evolution in the superplastic deformation of Ti75 alloy. *Materials Science Forum*, Vol. 475, 2005, pp. 2969–2972.

[3] Li, G. and S. Cui. A review on theory and application of plastic meso-damage mechanics. *Theoretical and Applied Fracture Mechanics*, Vol. 109, 2020, id. 102686.

[4] Cao, T., C. Bobadilla, P. Montmitonnet, and P. O. Bouchard. A comparative study of three ductile damage approaches for fracture prediction in cold forming processes. *Journal of Materials Processing Technology*, Vol. 216, 2015, pp. 385–404.

[5] Lemaitre, J. Local approach of fracture. *Engineering Fracture Mechanics*, Vol. 25, No. 5–6, 1986, pp. 523–537.

[6] Tvergaard, V. and A. Needleman. Analysis of the cup-cone fracture in a round tensile bar. *Acta metallurgica*, Vol. 32, No. 1, 1984, pp. 157–169.

[7] Bahrami, H., S. H. Hoseini, and G. Voyiadjis. Fracture investigation of the shape memory alloy using GTN model. *Engineering Fracture Mechanics*, Vol. 216, 2019, id. 106519.

[8] Zhai, J., T. Luo, X. Gao, S. Graham, M. Baral, Y. Korkolis, et al. Modeling the ductile damage process in commercially pure titanium. *International Journal of Solids and Structures*, Vol. 91, 2016, pp. 26–45.

[9] Qiang, B. and X. Wang. Ductile crack growth behaviors at different locations of a weld joint for an X80 pipeline steel: a numerical investigation using GTN models. *Engineering Fracture Mechanics*, Vol. 213, 2019, pp. 264–279.

[10] Breig, S. and K. Luti. Response surface methodology: a review on its applications and challenges in microbial cultures. *Materials Today: Proceedings*, Vol. 42, 2021, pp. 2277–2284.

[11] Manjakuppam, M. and S. Shriram. Application of RSM and ANN for the prediction and optimization of thermal conductivity ratio of water-based Fe2O3 coated SiC hybrid nanofluid. *International Communications in Heat and Mass Transfer*, Vol. 126, 2021, id. 105354.

[12] Mansouri, L., H. Chalal, and F. Abed-Meraim. Ductility limit prediction using a GTN damage model coupled with localization bifurcation analysis. *Mechanics of Materials*, Vol. 76, 2014, pp. 64–92.

[13] Slimane, A., B. Bouchouicha, M. Benguediab, and S. Slimane. Parametric study of the ductile damage by the Gurson–Tvergaard–Needleman model of structures in carbon steel A48-AP. *Journal of Materials Research and Technology*, Vol. 4, No. 2, 2015, pp. 217–223.

[14] Needleman, A. and V. Tvergaard. An analysis of ductile rupture in notched bars. *Journal of the Mechanics and Physics of Solids*, Vol. 32, No. 6, 1984, pp. 461–490.

[15] Benseddiq, N. and A. Imad. A ductile fracture analysis using a local damage model. *International Journal of Pressure Vessels and Piping*, Vol. 85, No. 4, 2008, pp. 219–227.

[16] Kami, A., B. Dariani, A. Vanini, D. Comsa, and D. Banabic. Numerical determination of the forming limit curves of anisotropic sheet metals using GTN damage model. *Journal of Materials Processing Technology*, Vol. 216, 2015, pp. 472–483.

[17] Parvez, W., K. Vijay, and L. Rahul. Flatness optimization of Zirconia ceramic material employing response surface methodology. *International Journal for Research in Engineering Application & Management*, Vol. 11, No. 5, 2020, pp. 86–88.

[18] Quan, G., G. Li, T. Chen, Y. Wang, Y. Zhang, and J. Zhou. Dynamic recrystallization kinetics of 42CrMo steel during compression at different temperatures and strain rates. *Materials Science and Engineering: A*, Vol. 528, No. 13–14, 2011, pp. 4643–4651.

[19] Soufen, C., M. Campos, and C. Pintao. Study of elastic properies of Ti3Al intermetallic compound using the Ab initio calculation. *Materials Science Forum*, Vol. 805, 2014, pp. 690–693.

[20] Shouqi, C., H. Xin, and L. Wanrong. Study on laser welding technology and properties of Ti75 titanium alloy. *Journal of Physics: Conference Series*, Vol. 16, No. 22, 2020, id. 012046.

[21] Abbassi, F., T. Belhadj, S. Mistou, and A. Zghal. Parameter identification of a mechanical ductile damage using artificial neural networks in sheet metal forming. *Materials & Design*, Vol. 45, 2013, pp. 605–615.

[22] Bonora, N., D. Gentile, A. Pirondi, and G. Newaz. Ductile damage evolution under triaxial state of stress: theory and experiments. *International Journal of Plasticity*, Vol. 21, No. 5, 2005, pp. 981–1007.